ChemCatChem

Research Article
doi.org/10.1002/cctc.202201691

Chemistry
Europe
European Chemical
Societies Publishing

www.chemcatchem.org

Calcium-Modified PtSn/Al$_2$O$_3$ Catalyst for Propane Dehydrogenation with High Activity and Stability

Xin-Qian Gao,[a] Zi-Hao Yao,[b] Wen-Cui Li,[a] Gao-Ming Deng,[a] Lei He,[a] Rui Si,*[c] Jian-Guo Wang,*[b] and An-Hui Lu*[a]

Catalytic dehydrogenation of propane to propylene and by-product hydrogen is an atom-economical and environmentally friendly route. PtSn/Al$_2$O$_3$ catalysts have been industrialized in this process, but still suffer from platinum sintering and coke deposition under reaction conditions. Herein, we design a calcium-modified PtSn/Al$_2$O$_3$ catalyst showing a superior propane dehydrogenation performance. The presence of calcium combined with unsaturated aluminum and tin could consist of a new local microenvironment that promotes the dispersion of the platinum species and increases the electron density of the platinum species, which improves the catalytic activity, facilitates propylene desorption and inhibits coke formation. As a result, the achieved PtSnCa/Al$_2$O$_3$ catalyst exhibits a higher propylene formation rate and a lower coke-accumulation rate compared to the catalyst without Ca addition. Moreover, the size of active phase clusters ($\sim$1 nm) remained almost unchanged after the catalytic test, indicating a superior sintering resistance.

Introduction

Propane dehydrogenation (PDH), an important industrial route for producing propylene, can effectively alleviate the over-dependence of propylene raw material on petroleum resources. This process supplies about 10% of the global propylene production, and the proportion is expected to increase significantly in the upcoming years with the success of the large-scale exploitation of shale gas.[1–4] Al$_2$O$_3$-supported Pt or CrOx catalyst has been commercially used in the PDH process depending on different production technologies.[5–7]

For the moment, the Pt-based catalysts become a preferential choice due to the tighter environmental regulations about Cr (VI) compounds. Owing to the thermodynamically limited and highly endothermic, high reaction temperatures are required to obtain sufficient propylene yields. Under such conditions, platinum species on the surface of alumina usually migrate to form large nanoparticles, consequently resulting in a decrease in catalytic activity and accelerating unavoidable coke formation.[1] The spent catalysts generally require frequent time- and energy-consuming regeneration, further accelerating a permanent deactivation caused by Pt sintering.[8–10] Hence, the catalytic processes generally require catalyst regenerations through high-temperature oxychlorination. In this case, the use of corrosion-resistant metallurgy for reactor design and an additional process to eliminate corrosive chlorine compounds are mandatory.[9–14] Therefore, the regulation of Pt-based catalysts with stabilized Pt atomic center is so far still a great challenge and always a desired point both in industrial and academic circles.

The alloying of platinum with promoter elements (e.g., Sn, Cu, Zn, Ga, In, etc.) is an alternative method to modify the electronic and geometric properties of platinum species.[15–24] In these cases, the promoter element can transfer electrons to the 5d band of platinum atoms, attenuating the adsorption of the product alkene to inhibit coke formation. Besides, platinum particles can be diluted to smaller platinum ensembles, and the reduction in the amount of near-neighbor Pt atoms within the ensembles will suppress those structure-sensitive side reactions, and thus inhibit the formation of coke. However, due to the promoter partially covering active platinum sites and meanwhile pushing down the d band center of platinum, the alloying catalysts significantly lower the reaction rate of propane dehydrogenation, where the catalytic activity is compromised.[25–27]

The Al$_2$O$_3$-supported Pt–Sn catalysts have been successfully commercialized in the Oleflex process developed by the UOP company. Although it has been suggested that the addition of Sn can inhibit the agglomeration of Pt species, the sintering of the Pt nanoparticles during the harsh dehydrogenation and/or regeneration processes is still an unsolved fatal issue.[12,25,28–31] Furthermore, the rational design of the support structure is another useful way to modulate the electronic and geometric structure of active metal phases. Mironenko et al. reported that

[a] X.-Q. Gao, W.-C. Li, G.-M. Deng, L. He, Prof. A.-H. Lu
State Key Laboratory of Fine Chemicals
School of Chemical Engineering
Dalian University of Technology
Dalian 116024 (P. R. China)
E-mail: anhuilu@dlut.edu.cn

[b] Z.-H. Yao, J.-G. Wang
Shanghai Synchrotron Radiation Facility
Shanghai Institute of Applied Physics
Chinese Academy of Sciences
Shanghai 201204 (P. R. China)
E-mail: jgw@zjut.edu.cn

[c] R. Si
State Key Laboratory Breeding Base of Green-Chemical Synthesis Technology
College of Chemical Engineering
Zhejiang University of Technology
Hangzhou 310032 (P. R. China)
E-mail: sirui@mail.sysu.edu.cn

Supporting information for this article is available on the WWW under https://doi.org/10.1002/cctc.202201691

ChemCatChem

Research Article
doi.org/10.1002/cctc.202201691

Chemistry Europe
European Chemical
Societies Publishing

hydrothermally treated γ-alumina can alter the metal complex-support interaction, thus changing the dispersion and electronic state of supported platinum to improve the catalytic performance.[32] In our previous study, we synthesized a γ-alumina nanosheet that is rich in pentacoordinate Al^{3+} ions, which can act as anchoring sites to effectively disperse and stabilize Pt–Sn clusters.[33] However, the origin of its efficient catalytic behavior in propane dehydrogenation has not been well understood at the atomic level.

Herein, we report that a designed $PtSnCa/Al_2O_3$ catalyst with superior propane dehydrogenation performance benefited from the regulation of the platinum active phase microenvironment. The achieved $PtSnCa/Al_2O_3$ catalyst exhibits a high propylene formation rate and superior sintering resistance and anti-coking ability with a very low coke-accumulation rate compared to the catalyst without Ca addition. The microenvironment regulation for the active phase through the rational design of proximal atoms provides guidelines for the future design of noble metal catalysts with high reactivity and stability for a variety of catalytic applications.

Results and discussion

Catalytic performance

Propane dehydrogenation was tested using a feed stream of 16 vol.% C_3H_8, 20 vol.% H_2, and N_2 balance with a space velocity of 9.4 $g_{C3H8}\,g_{cat}^{-1}\,h^{-1}$ at 590 °C and 1 bar. As shown in Figure 1A, the dependence of propane conversion and propylene selectivity over the Pt/Al_2O_3, $PtSn/Al_2O_3$, and $PtSnCa/Al_2O_3$ catalysts on the reaction time. The $PtSnCa/Al_2O_3$ catalyst exhibited significantly enhanced in terms of reactivity and stability during the 24-hour PDH reaction in comparison to the other catalyst. An initial propane conversion of 54% was achieved with 98.7% selectivity for propylene. The specific activity of propylene formation over the $PtSnCa/Al_2O_3$ catalyst was 1.67 $mol_{C3H6}\,mol_{Pt}^{-1}\,s^{-1}$, which was better than 1.27 $mol_{C3H6}\,mol_{Pt}^{-1}\,s^{-1}$ for monometallic Pt/Al_2O_3 catalyst and 1.57 $mol_{C3H6}\,mol_{Pt}^{-1}\,s^{-1}$ for the bimetallic $PtSn/Al_2O_3$ catalyst (Table S2). After a 24-hour dehydrogenation reaction, propylene selectivity improved to 99.1% at 48.8% propane conversion. Furthermore, the PDH was also tested under a higher space velocity to push the conversion of propane away from the equilibrium conversion (Figure S1). With an increase in space
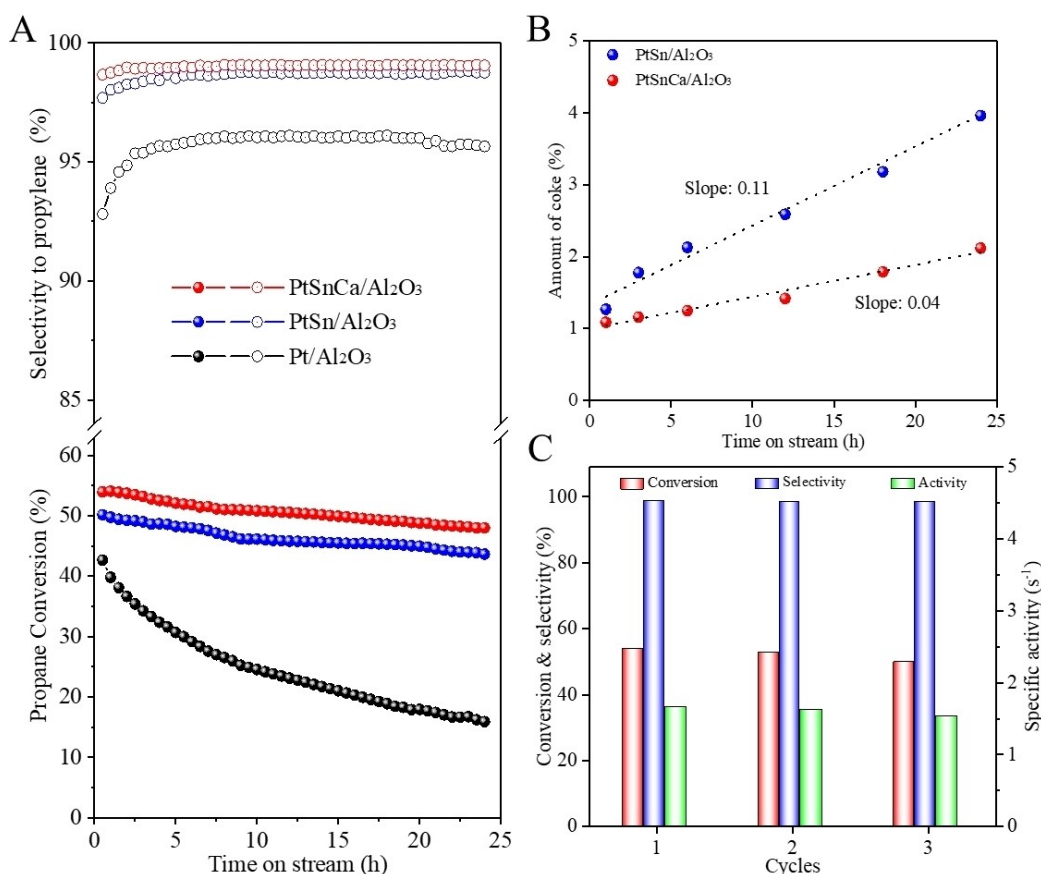

Figure 1. Catalytic performance of $PtSnCa/Al_2O_3$ catalyst. (A) The dependence of propane conversion and propylene selectivity on reaction time. (B) Amount of coke deposits as a function of dehydrogenation reaction time. (C) Initial propane conversion, propylene selectivity, and specific activity of propylene formation during 3 consecutive dehydrogenation-regeneration cycles. Catalytic conditions: atmospheric pressure, 590 °C, $C_3H_8/H_2 = 1/1.25$, with balance N_2 for total flow rate of 50 mL min^{-1}, WHSV of propane = 9.4 h^{-1} over 100 mg of sample. The spent catalyst is regenerated at 500 °C under an air stream for 120 min, and the flow rate of air was 40 mL min^{-1}.

velocity from $9.4\ h^{-1}$ to $75.2\ h^{-1}$, the initial propane conversion over $PtSnCa/Al_2O_3$ catalyst decreased to 29.5%, the initial propylene selectivity increased to 99.0%, and the specific activity of propylene formation increased to $7.31\ mol_{C3H6}\ mol_{Pt}^{-1}\ s^{-1}$, all of which were better than the catalyst without Ca addition. We have evaluated the influence of the calcium content on catalytic performance, the propane conversion exhibited a volcanic curve with the calcium content increasing, reaching a maximum at a loading of 0.5% (Figure S2A). Small amounts of calcium have insignificant effects on catalytic performance, while excessive calcium may cover the active site resulting in decreased catalytic activity. Furthermore, we also evaluated the PDH performances of lithium, sodium, potassium, magnesium, and barium-modified $PtSn/Al_2O_3$ catalysts, where the additive loading was maintained at 0.5%. As shown in Figure S3, all these additives on these catalysts showed a negative effect on the propane activation in the PDH reaction, which may be due to unsuitable properties or loading amounts. Thus, calcium additives with appropriate ratios have a unique promotional role of calcium in such catalyst configurations. To further evaluate the catalyst stability, a first-order deactivation model was used to calculate the deactivation parameters of the catalyst. As shown in Table S2–3, the as-prepared catalyst had superior reactivity and stability with high specific activity and low deactivation rate outperformed those reported Al_2O_3-supported Pt-based catalysts. It was important to highlight that the calcium-modified $PtSn/Al_2O_3$ catalyst exhibited superior coke-resistant capability. The TG measurement in the TPO mode revealed that the amount of coke deposits on the spent catalysts was significantly decreased with the introduction of calcium. As exemplified by intuitive photography images, the color of the spend $PtSnCa/Al_2O_3$ catalyst changed from black to grey with the introduction of 0.5 wt% calcium, and the amount of coke was reduced from 3.70% to 2.12% (Figure S2B). A correlation between coking amount and dehydrogenation time was established to determine the coke-accumulation rates of the catalysts (Figure 1B).

$PtSnCa/Al_2O_3$ catalyst possessed a very low coke-accumulation rate ($0.04\ h^{-1}$), which decreased by more than 60% compared to the catalyst without Ca addition. Furthermore, three successive dehydrogenation-regeneration cycling over the fresh $PtSnCa/Al_2O_3$ catalyst were investigated to examine the durability under harsh operating conditions (Figure 1C). Only a slight decrease in propane conversion was observed, while the propylene selectivity remained essentially unchanged at high temperatures. The conversion and selectivity of the $PtSnCa/Al_2O_3$ catalyst were always higher than that of the $PtSn/Al_2O_3$ catalyst during the three successive dehydrogenation-regeneration cycles (Figure S4). All these results clearly demonstrated that the modification of calcium can enhance the PDH reactivity and stability, especially the coke-resistant ability of the alumina-supported platinum-tin catalysts.

Textural and surface properties of catalysts

To clarify the unique promotional role of calcium on PDH reactivity and coking behavior, we initially investigated the effect of calcium modification on the catalyst texture and surface property (Table S1). One can see that the calcium modification leads to a ~6% decrease in the catalyst surface area. The NH_3-TPD measurement showed that the calcium addition had little effect on the acidity of the catalyst surface ($330\ \mu mol/g_{cat}$ on $PtSn/Al_2O_3$ versus $314\ \mu mol/g_{cat}$ on $PtSnCa/Al_2O_3$), and the relative proportion of weak, modest, and strong acid also remained invariable (Figure 2A), which was distinguished from the usual viewpoints that the basic component will effectively neutralize the acidic sites on the Al_2O_3 surface.[34–36] Furthermore, a CO_2-TPD study was carried out to evaluate the change of catalyst surface basicity after calcium modification. As shown in Figure 2B, the two samples exhibited a similar desorption peak of CO_2 at ~120°C, corresponding to hydroxyl groups on the Al_2O_3 surface.[37] And the CO_2 desorption at 300~700°C attributed to the interaction with the $Ca^{2+}-O^{2-}$
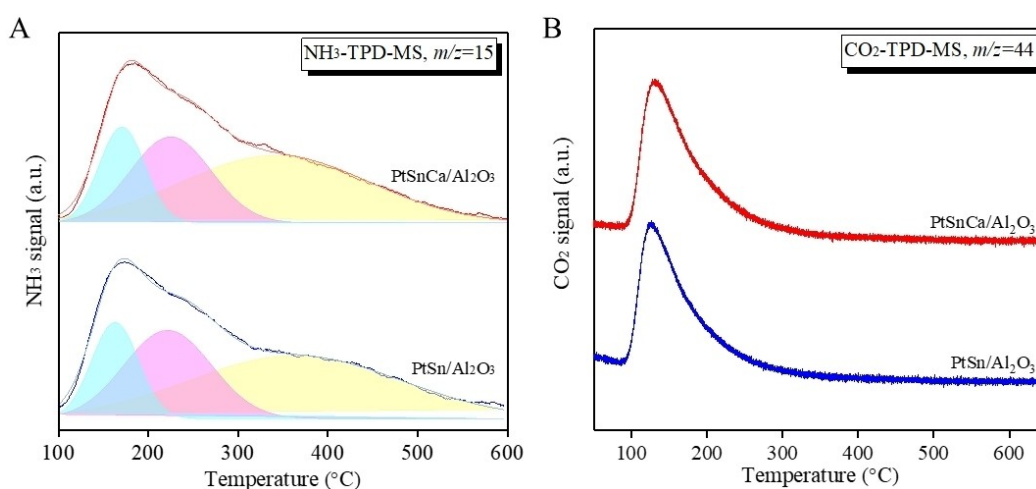
Figure 2. Acid-base properties of catalyst. (A) NH_3-TPD profile of the $PtSn/Al_2O_3$ and $PtSnCa/Al_2O_3$ catalysts. (B) CO_2-TPD profile of the $PtSn/Al_2O_3$ and $PtSnCa/Al_2O_3$ catalysts.

pair on the Al_2O_3 surface was not found.[38] Therefore, the inhibition of coke formation by calcium additive was derived from the modification of the active phase rather than the support surface.

Geometry and electronic properties of platinum species before and after PDH reaction

To understand the outstanding reactivity and stability of the Pt-based catalysts, we carefully tracked the evolution of catalyst structure before ("initial") and after ("final") reaction. Aberration-corrected high-angle annular dark field-scanning transmission electron microscopy (HAADF-STEM) measurements were conducted to reveal the atomic-resolution structure of the catalysts (Figure 3A and Figure S5–7). We observed small low-dimensional clusters as well as a number of loose ensembles on the surface of the Al_2O_3 nanosheet with an average size of approximately 1 nm, which was smaller than the PtSn clusters on the Al_2O_3 nanosheet ($\sim$ 1.3 nm). The energy-dispersive X-ray spectroscopy (EDX) elementary maps revealed the spatial distribution of the Pt, Sn, and Ca on the support surface (Figure 3E). By comparing spatial features in Pt, Sn, and Ca maps, it was apparent that there was a large degree of correlation between the location of the Pt, Sn, and Ca elements because regions of higher Pt and Sn intensities appear at regions of higher Ca intensity, suggesting that the close association of three components consists of the catalytically active phase attached on the surface of Al_2O_3. It's well known, in heterogeneous catalysis, the topmost atomic layer of the catalyst is the precise location where the catalytic process takes place. Considering that only the bulk information is provided by EDS analysis, the high sensitivity-low energy ion scattering (HS-LEIS), which is a sensitive analysis technique for the outermost atomic layer of a sample, was further used to detect the surface region of the calcium-promoted platinum-tin active phase. As shown in Figure S8, it was clear that Pt, Sn, and Ca co-exist on the outmost surface, and comprise the multicomponent active phase supported on the Al_2O_3 surface. In more detail, high-magnification Z-contrast micrographs (Figure 3A) showed that the primary species on the support surface were discrete clusters with sub-nanometer diameters. Longitudinal annular dark-field (ADF) intensity was normalized to obtain more insights into the three-dimensional structure of these clusters. An intensity comparison (Figure 3B) between two representative clusters (No. 1 and 2, see Figure 3A) clearly indicated the thickness of these clusters with sub-nanometer diameter was one to two atomic layers. Further statistical analysis (Figure 3D) of more than 80 clusters revealed that the clusters with a thickness of 1- or 2-layer amount to 94%. From the perspective of width and thickness, Figure 3C provided convincing evidence for the presence of sub-nanometer clusters predominantly in the $PtSnCa/Al_2O_3$ catalyst. These observations indicated that PtSnCa clusters were well dispersed and stabilized on the alumina surface. Therefore, the decrease in the active phase cluster size benefited the exposure of more active sites to improve the catalytic activity, and the strong metal-support interactions facilitated the improvement of the sintering resistance.

To characterize the chemical environment and electronic properties of platinum species in the catalysts, X-ray absorption fine structure (XAFS) spectra were collected. The k^2-weighted Fourier transform of extended X-ray absorption fine structure of Pt L_3 edge of the Pt catalysts and the standard references (Pt-foil and PtO_2) were shown in Figure 4A. As compared with Pt-foil and PtO_2, a similar peak near 2.01 Å in EXAFS spectra for all Pt catalysts could be ascribed to the Pt–O coordination.[39–41] As the catalysts were pre-reduced before the measurements, the presence of PtO_x phases could in principle be ruled out in samples.[42] However, we observed a bond distance close to that in PtO_2, indicating the presence of Pt–O bond which was ascribed to the strong interaction of platinum with the support. Further quantitative analysis of the coordination structure was conducted by the fitting of R space of Pt-based catalysts (Table S4). In the $PtSnCa/Al_2O_3$ catalyst, the Pt–Pt bonding distance of 2.75 Å with a coordination number of 0.9, which was slightly lower than that of the $PtSn/Al_2O_3$ catalyst, and the former possessed more coordinating neighbors of Pt–O, implying the platinum species had a better dispersion with the presence of calcium promoter, which was consistent with the decrease in particle size in the HAADF-STEM result. After 24-hour propane dehydrogenation, the corresponding Pt–O coordination number decreased with the simultaneous disappearance of Pt–Pt bond and appearance of Pt–Sn bond, suggesting the existence of structure evolution under reaction conditions. The EXAFS data did not reveal any Pt–Pt presence in spent catalysts, indicating there might be only isolated Pt sites contained in the catalyst. Compared to $PtSn/Al_2O_3$ catalyst, both the coordination number and bonding distance of Pt–Sn decreased in $PtSnCa/Al_2O_3$ catalyst, revealing the different interaction between platinum and tin species. Given that the Ca addition was the only difference, such changes in the local coordination environment must originate from the calcium modulation.

With an understanding on geometric configuration, the chemical properties of platinum species were further evaluated by combining the X-ray absorption near-edge structure. Prior to detect Pt, the electronic state of tin and calcium species was identified via the XPS measurement. As shown in Figure S9A, the Sn 3d XPS spectra confirmed that the prevailing valence of tin species was $+2$ in $PtSn/Al_2O_3$ and $PtSnCa/Al_2O_3$ catalysts.[33,43,44] Different from that reported in the literature where the addition of calcium favored the reduction of tine species,[36] the same binding energy in both catalysts indicated that there was no interaction between the tin species and the calcium promoter in the $PtSnCa/Al_2O_3$ catalyst. As shown in Figure S9B, the Ca 2p XPS spectra demonstrated a principal peak at 345.4 eV with a shoulder peak at 348.8 eV, indicating that calcium species were in an oxidized state.[45] Combined the XPS and CO_2-TPD measurements demonstrated that calcium species were present in the cationic form.[37,46] The normalized profiles revealed that the edge energy and white line intensities of all Pt catalysts were similar to platinum foil (Figure 4B), indicating that the platinum species were in a metallic state in
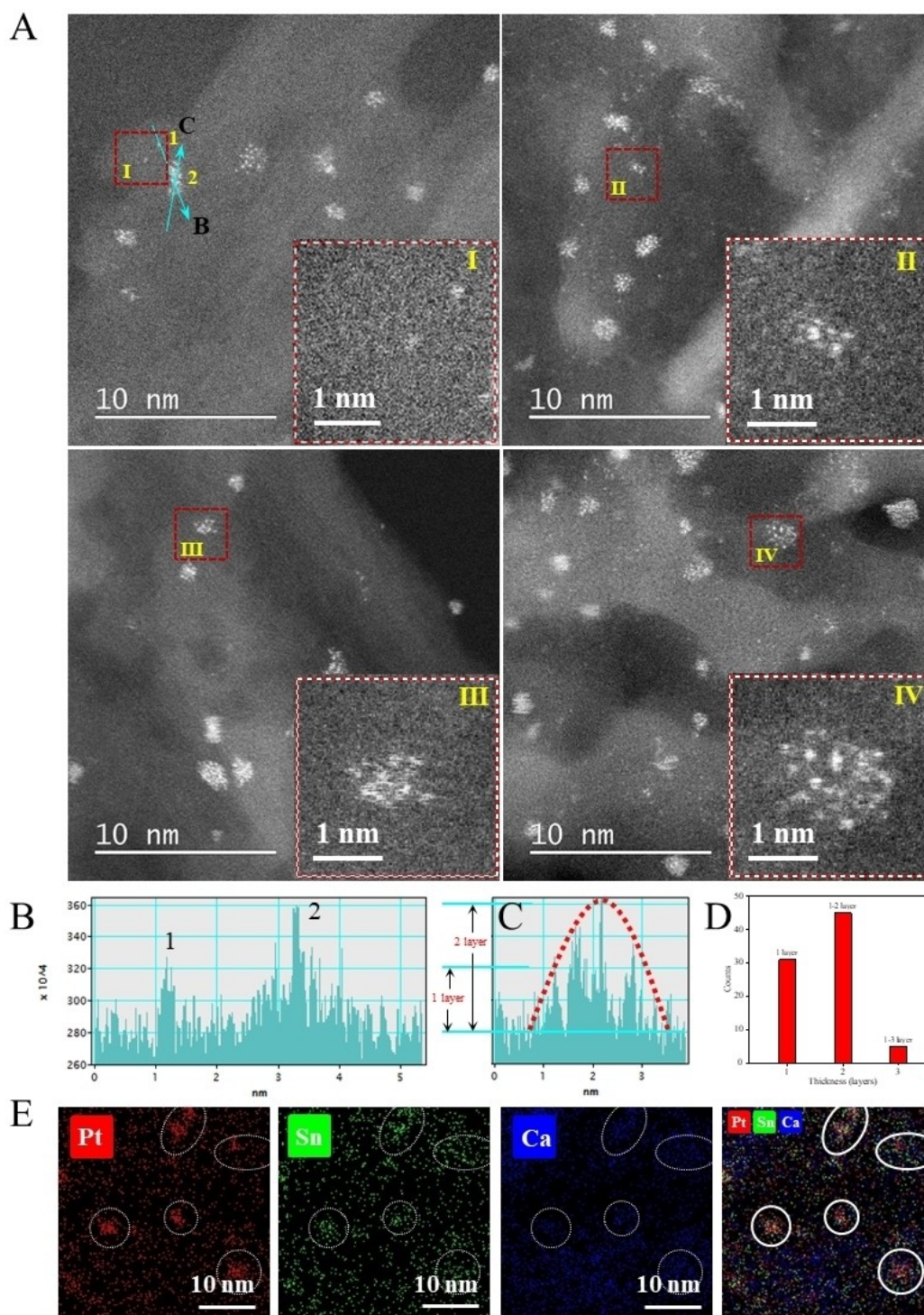
Figure 3. Structural features of PtSnCa/Al$_2$O$_3$ catalyst. (A) Aberration-corrected HAADF-STEM images. (B and C) ADF intensity along the blue line in the A image. (D) Height distribution of 81 selected clusters determined from the relative intensities of Z-contrast images. (E) Two-dimensional elemental maps using STEM-EDX imaging analysis of representative PtSnCa/Al$_2$O$_3$ catalyst.

these catalysts..[25,42,47] The CO-DRIFT spectra of the PtSnCa/Al$_2$O$_3$ catalyst and reference samples at 573 K demonstrated strong interaction between Pt sites and CO, which was consistent with the above conclusion (Figure 4C). Moreover, the result of the C$_3$H$_6$-TPD experiment in Figure S10 showed that the desorption

temperature of electron-rich propylene over the PtSnCa/Al$_2$O$_3$ sample (135 °C) was lower in comparison with that over the PtSn/Al$_2$O$_3$ sample (186 °C), indicating that the electronic density of platinum increases in PtSnCa/Al$_2$O$_3$ catalyst. The higher electron density of platinum species will attenuate the

ChemCatChem

Research Article
doi.org/10.1002/cctc.202201691

Chemistry
Europe
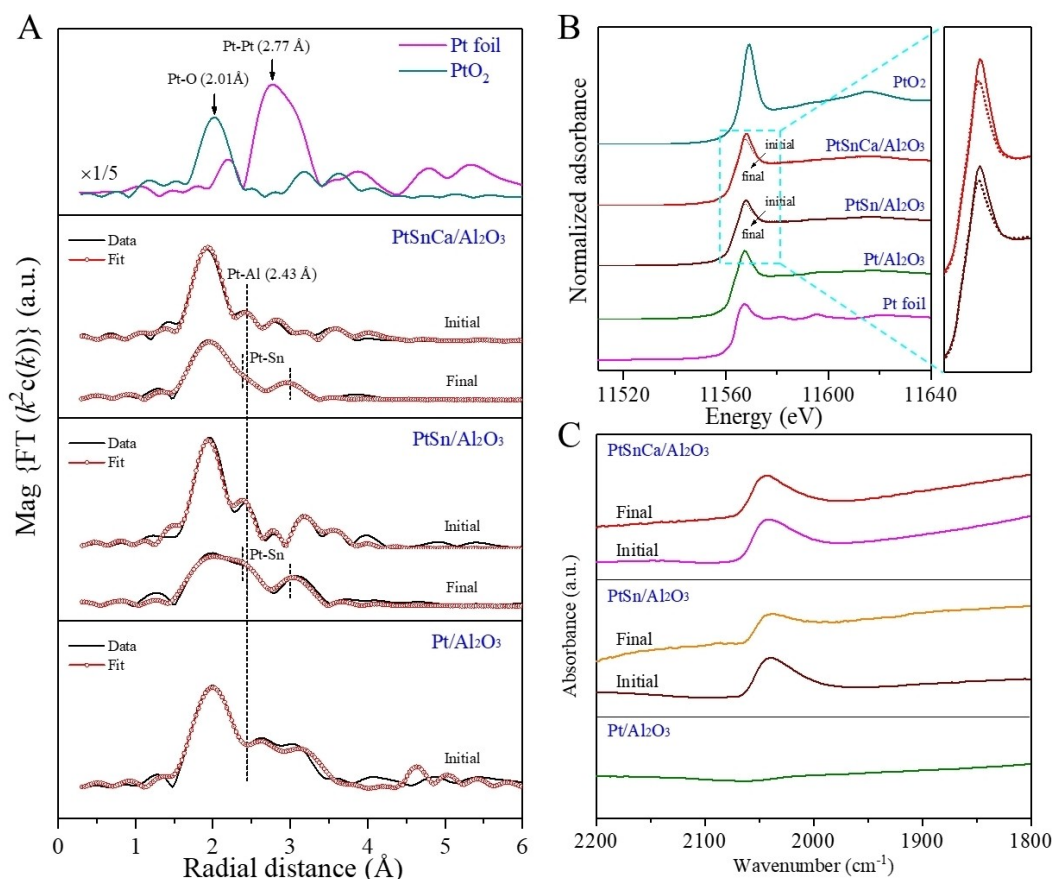European Chemical
Societies Publishing

Figure 4. Chemical environment and electronic properties of platinum species. (A) Fourier transform of the Pt LIII-edge EXAFS spectra of the PtSnCa/Al$_2$O$_3$ catalyst and reference samples. (B) Normalized XANES profiles at the Pt L$_{III}$-edge of the PtSnCa/Al$_2$O$_3$ catalyst and reference samples. (C) CO-DRIFT spectra of the PtSnCa/Al$_2$O$_3$ catalyst and reference samples at 573 K.

adsorption of the product alkene to inhibit coke formation,[26,27] which was a good explanation for the excellent anti-coking ability of the PtSnCa/Al$_2$O$_3$ catalyst. After 24-hour propane dehydrogenation, the white line intensities at the Pt L$_3$ edges decreased, suggesting the increase in the electronic density of platinum species.[20,47–49] The platinum species in these catalysts became much more electron-rich after exposure to the reaction mixtures, confirming the structural evolution of platinum species occurs under the reaction conditions. It was noteworthy that the decline in white line intensity of the PtSnCa/Al$_2$O$_3$ catalyst was more obvious, suggesting further enhancement of the charge transfer between platinum and microenvironment by the addition of calcium. These results manifested that the structure of the active phase evolved under the reaction conditions, and the addition of calcium effectively regulated the evolution process.

Conclusions

In summary, we have developed a novel PtSnCa/Al$_2$O$_3$ catalyst with a unique microenvironment exhibiting high selectivity, high specific activity, low coke-accumulation rate, and superior sintering resistance in the catalytic dehydrogenation of the propane process. The addition of calcium promoted the dispersion of platinum species and boosted the charge transfer between platinum and its microenvironment, contributing to a high specific activity of propylene formation and a low coke-accumulation rate. This study demonstrates that microenvironment regulation for the active phase through the rational association of proximal atoms provides a new strategy for the design of heterogeneous catalysts.

Experimental

Support preparation. The γ-Al$_2$O$_3$ nanosheet support was synthesized according to our previous work.[33] Typically, suitable amounts of Al(NO$_3$)$_3$·9H$_2$O and CO(NH$_2$)$_2$ were dissolved in deionized water and then placed in a Teflon-lined stainless autoclave and maintained at 100 °C for 48 h. After air-cooling to room temperature, the obtained white precipitate was filtered and washed with deionized water and anhydrous alcohol several times and then dried overnight at 80 °C. Finally, γ-Al$_2$O$_3$ nanosheet was obtained by calcination of the powder in air at 600 °C for 2 h with a heating rate of 1 °C/min.

Catalysts preparation. Platinum-tin-calcium supported γ-Al$_2$O$_3$ nanosheet catalysts (PtSnCa/Al$_2$O$_3$) were prepared using the incipient co-impregnation method with H$_2$PtCl$_6$·6H$_2$O, SnCl$_2$·2H$_2$O, and Ca(NO$_3$)$_2$·4H$_2$O as the precursors. Typically, the solution

containing the three metal precursors was incipient impregnated into the alumina nanosheet support. Subsequently, the impregnated samples were maintained at room temperature for 2 h and then dried overnight at 50 °C. Finally, the catalysts were calcined at 500 °C for 4 h and then reduced in 20 % H_2/N_2 atmosphere at 590 °C for 2 h. As compared, the Pt/Al_2O_3, $PtSn/Al_2O_3$, and $PtSnM/Al_2O_3$ (M represents various metals) were prepared by the same procedures of the $PtSnCa/Al_2O_3$ catalyst.

Catalyst characterization. The actual loading of platinum, tin, and calcium was identified by inductively coupled plasma optical emission spectroscopy (ICP-OES). The textural properties were measured with a Micromeritics TriStar 3000 adsorption analyzer. The amount of coke deposited was measured with a thermogravimetric (TG) analyzer STA 449 F3 (NETZSCH). Temperature-programmed experiments were performed on a Micromeritics AutoChem II 2920 apparatus with a TCD detector and/or a mass spectrometer. Aberration-corrected high-angle annular dark-field scanning transmission electron microscopy (HAADF-STEM) images and energy dispersive X-ray (EDX) spectroscopy were obtained on a JEOL JEM-2100 microscope operated at an accelerating voltage of 200 kV. Diffuse reflectance infrared Fourier transform (DRIFT) spectra were recorded on a Bruker 70 V spectrometer with an in situ reaction cell (HARRICK) and MCT detector. X-ray photoelectron spectroscopy (XPS) analysis was performed on an Omicron Sphera II hemispherical electron energy analyzer with an in-situ reaction cell. Before the measurements, all the samples were reduced at 590 °C for 1 h in 20 % H_2/N_2 atmosphere and then moved to the measured chamber under vacuum conditions. The binding energy of the element was calibrated using a C 1s photoelectron peak at 284.6 eV. High sensitivity-low energy ion scattering (HS-LEIS) measurement was performed on an IonTOF Qtac100 low-energy ion scattering analyzer. He^+ ions with a kinetic energy of 3 keV were applied at a low ion flux equal to 1325 pA cm^{-2}. Ne^+ ions with a kinetic energy of 5 keV were applied at a low ion flux equal to 445 pA cm^{-2}. Quasi-in-situ X-ray absorption fine structure (XAFS) spectra at Pt L_3 ($E_0 = 11564.0$ eV) edge were performed at BL14 W1 beamline of Shanghai Synchrotron Radiation Facility (SSRF) operated at 3.5 GeV under "top-up" mode with a constant current of 250 mA. A Si (111) double-crystal monochromator was used to reduce the harmonic component of the monochrome beam. All the samples were measured in the fluorescence mode with a Lytle-type ion chamber. Before measurements, the powder sample was pre-reduced at 590 °C for 1 h in 20 % H_2/N_2 atmosphere in a specially designed reactor equipped with shut-off valves at both ends. Prior to disconnection with the flowing hydrogen, the valves on the reactor were closed so that the freshly reduced sample was not exposed to air. After that, the reactor was transferred into an argon-filled glove box. Specimens were made by directly applying the fine powders to scotch tape under a vacuum package, sealed by the valve bag. The energy was calibrated accordingly to the absorption edge of pure Pt foil. Athena and Artemis codes were used to extract the data and fit the profiles. For the X-ray absorption near edge structure (XANES) part, the experimental absorption coefficients as function of energies $\mu(E)$ were processed by background subtraction and normalization procedures, and reported as "normalized absorption" with $E_0 = 11564.0$ eV for all the measured samples and references. For the extended X-ray absorption fine structure (EXAFS) part, the Fourier transformed (FT) data in R space were analyzed by applying PtO_2, metallic Pt and first-shell approximate models for Pt–O, Pt–Pt Pt–Al/Pt–Sn/Pt–Pt (from Pt–O–Pt) contributions, respectively. The passive electron factors, S_0^2, were determined by fitting the experimental data on Pt foils and fixing the coordination number (CN) of Pt–Pt to be 12, and then fixed for further analysis of the measured samples. The parameters describing the electronic properties (e.g., correction to the photoelectron energy origin, E_0)

and local structure environment including CN, bond distance (R) and Debye-Waller factor around the absorbing atoms were allowed to vary during the fit process. The fitted ranges for k and R spaces were selected to be $k = 3$–11 Å^{-1} with $R = 1.1$–4.0 Å (k^2 weighted).

Catalytic evaluation. Catalytic performance was tested in a tubular fixed-bed quartz reactor (I. D. = 8 mm, length = 42 cm) packed with 100 mg catalyst (the particle size of catalyst is 40~60 mesh). Before the reactivity test, the catalyst was first heated to 590 °C with a rate of 10 °C min^{-1} and retained at 590 °C for 2 h in flowing 20 vol % H_2/N_2. During the activity test, the reaction mixture of 16 vol % C_3H_8 and 20 vol % H_2 and N_2 balance was fed at a total flow of 50 mL min^{-1}, where the gas flow rates were 8 ml min^{-1}, 10 ml min^{-1}, and 32 ml min^{-1}, respectively. After the dehydrogenation reaction in each cycle, the spent catalyst was regenerated by treatment in air at 500 °C for 120 min, and the flow rate of air was 40 mL/min. The products were analyzed by an on-line gas chromatograph. GDX-105 and molecular sieve 5 A columns were used to analyze the N_2, C_3H_8, C_3H_6, C_2H_4, C_2H_6, and CH_4 in the products. The propane conversion and propylene selectivity were calculated using the following equations and the carbon balance was generally higher than 97 % (Eqs. 1–3).

$$C_{C_3H_8} = \left[\frac{F_{in}\,(C_3H_8)}{F_{in}\,(N_2)} - \frac{F_{out}\,(C_3H_8)}{F_{out}\,(N_2)}\right] / \left[\frac{F_{in}\,(C_3H_8)}{F_{in}\,(N_2)}\right] \quad (1)$$

$$S_{C_3H_6} = \left(3\,\frac{F_{out}\,(C_3H_6)}{F_{out}\,(N_2)}\right) / \left[\left(\frac{F_{out}\,(CH_4)}{F_{out}\,(N_2)}\right) + \left(2\,\frac{F_{out}\,(C_2H_6)}{F_{out}\,(N_2)}\right) + \left(2\,\frac{F_{out}\,(C_2H_4)}{F_{out}\,(N_2)}\right) + \left(3\,\frac{F_{out}\,(C_3H_6)}{F_{out}\,(N_2)}\right)\right] \quad (2)$$

$$Carbon\ balance = \left[\left(\frac{F_{out}\,(CH_4)}{F_{out}\,(N_2)}\right) + \left(2\,\frac{F_{out}\,(C_2H_6)}{F_{out}\,(N_2)}\right) + \left(2\,\frac{F_{out}\,(C_2H_4)}{F_{out}\,(N_2)}\right) + \left(3\,\frac{F_{out}\,(C_3H_6)}{F_{out}\,(N_2)}\right)\right] / \left[3\,\frac{F_{in}\,(C_3H_8)}{F_{in}\,(N_2)} - 3\,\frac{F_{out}\,(C_3H_8)}{F_{out}\,(N_2)}\right] \quad (3)$$

where i represents hydrocarbon products in the effluent gas stream, n_i is the number of carbon atoms of component i, and F(i) is the corresponding flow rate.

A first-order deactivation model was used to evaluate the catalyst stability (Eq. 4), and the derivation process is described in the Supplementary materials:

$$k_d = \left(ln\frac{1 - X_{final}}{X_{final}} - ln\frac{1 - X_{initial}}{X_{initial}}\right) / t \quad (4)$$

where $X_{initial}$ and X_{final}, respectively, represent the conversion measured at the the initial and final period of an experiment, and t represents the reaction time (h), k_d is the deactivation rate constant (h^{-1}). Higher k_d values are indicative of rapid deactivation, that is, low stability.

Acknowledgements

ChemCatChem

Research Article
doi.org/10.1002/cctc.202201691

**Chemistry
Europe**
European Chemical
Societies Publishing

Conflict of Interest

The authors declare that they have no known competing financial interests or personal relationships that could have appeared to influence the work reported in this paper.

Data Availability Statement

The data that support the findings of this study are available in the supplementary material of this article.

[1] J. J. Sattler, J. Ruiz-Martinez, E. Santillan-Jimenez, B. M. Weckhuysen, *Chem. Rev.* **2014**, *114*, 10613–10653.
[2] S. Chen, X. Chang, G. Sun, T. Zhang, Y. Xu, Y. Wang, C. Pei, J. Gong, *Chem. Soc. Rev.* **2021**, *50*, 3315–3354.
[3] W. Yan, Q. Sun, J. Yu, *Matter* **2021**, *4*, 2642–2644.
[4] Y. Gu, H. Liu, M. Yang, Z. Ma, L. Zhao, W. Xing, P. Wu, X. Liu, S. Mintova, P. Bai, Z. Yan, *Appl. Catal. B* **2020**, *274*, 119089.
[5] D. Sanfilippo, I. Miracca, *Catal. Today* **2006**, *111*, 133–139.
[6] B. V. Vora, *Top. Catal.* **2012**, *55*, 1297–1308.
[7] J. C. Bricker, *Top. Catal.* **2012**, *55*, 1309–1314.
[8] H.-Z. Wang, L.-L. Sun, Z.-J. Sui, Y.-A. Zhu, G.-H. Ye, D. Chen, X.-G. Zhou, W.-K. Yuan, *Ind. Eng. Chem. Res.* **2018**, *57*, 8647–8654.
[9] J. Im, M. Choi, *ACS Catal.* **2016**, *6*, 2819–2826.
[10] Z. Lian, C. Si, F. Jan, S. Zhi, B. Li, *ACS Catal.* **2021**, *11*, 9279–9292.
[11] H. C. Kwon, Y. Park, J. Y. Park, R. Ryoo, H. Shin, M. Choi, *ACS Catal.* **2021**, *11*, 10767–10777.
[12] H. N. Pham, J. J. Sattler, B. M. Weckhuysen, A. K. Datye, *ACS Catal.* **2016**, *6*, 2257–2264.
[13] G.-Q. Ren, G.-X. Pei, Y.-J. Ren, K.-P. Liu, Z.-Q. Chen, J.-Y. Yang, Y. Su, X.-Y. Liu, W.-Z. Li, T. Zhang, *J. Catal.* **2018**, *366*, 115–126.
[14] R. Ryoo, J. Kim, C. Jo, S. W. Han, J. C. Kim, H. Park, J. Han, H. S. Shin, J. W. Shin, *Nature* **2020**, *585*, 221–224.
[15] O. A. Bariås, A. Holmen, E. A. Blekkan, *Catal. Today* **1995**, *24*, 361–364.
[16] Q. Li, Z. Sui, X. Zhou, D. Chen, *Appl. Catal. A* **2011**, *398*, 18–26.
[17] G. Sun, Z. J. Zhao, R. Mu, S. Zha, L. Li, S. Chen, K. Zang, J. Luo, Z. Li, S. C. Purdy, A. J. Kropf, J. T. Miller, L. Zeng, J. Gong, *Nat. Commun.* **2018**, *9*, 4454.
[18] Z. Han, S. Li, F. Jiang, T. Wang, X. Ma, J. Gong, *Nanoscale* **2014**, *6*, 10000–10008.
[19] X. Li, Y. Zhou, B. Qiao, X. Pan, C. Wang, L. Cao, L. Li, J. Lin, X. Wang, *J. Energy Chem.* **2020**, *51*, 14–20.
[20] V. J. Cybulskis, B. C. Bukowski, H.-T. Tseng, J. R. Gallagher, Z. Wu, E. Wegener, A. J. Kropf, B. Ravel, F. H. Ribeiro, J. Greeley, J. T. Miller, *ACS Catal.* **2017**, *7*, 4173–4181.
[21] E. A. Redekop, V. V. Galvita, H. Poelman, V. Bliznuk, C. Detavernier, G. B. Marin, *ACS Catal.* **2014**, *4*, 1812–1824.
[22] P. Wang, J. Yao, Q. Jiang, X. Gao, D. Lin, H. Yang, L. Wu, Y. Tang, L. Tan, *Appl. Catal. B* **2022**, *300*, 120731.
[23] T. Wang, F. Jiang, G. Liu, L. Zeng, Z.-j. Zhao, J. Gong, *AIChE J.* **2016**, *62*, 4365–4376.
[24] W. Tolek, K. Suriye, P. Praserthdam, J. Panpranot, *Catal. Today* **2020**, *358*, 100–108.
[25] A. Iglesias-Juez, A. M. Beale, K. Maaijen, T. C. Weng, P. Glatzel, B. M. Weckhuysen, *J. Catal.* **2010**, *276*, 268–279.
[26] M.-L. Yang, Y.-A. Zhu, X.-G. Zhou, Z.-J. Sui, D. Chen, *ACS Catal.* **2012**, *2*, 1247–1258.
[27] L. Nykänen, K. Honkala, *ACS Catal.* **2013**, *3*, 3026–3030.
[28] A. W. Hauser, J. Gomes, M. Bajdich, M. Head-Gordon, A. T. Bell, *Phys. Chem. Chem. Phys.* **2013**, *15*, 20727–20734.
[29] H. Zhu, D. H. Anjum, Q. Wang, E. Abou-Hamad, L. Emsley, H. Dong, P. Laveille, L. Li, A. K. Samal, J.-M. Basset, *J. Catal.* **2014**, *320*, 52–62.
[30] N. Kaylor, R. J. Davis, *J. Catal.* **2018**, *367*, 181–193.
[31] Y. Zhu, Z. An, H. Song, X. Xiang, W. Yan, J. He, *ACS Catal.* **2017**, *7*, 6973–6978.
[32] R. M. Mironenko, O. B. Belskaya, V. P. Talsi, T. I. Gulyaeva, M. O. Kazakov, A. I. Nizovskii, A. V. Kalinkin, V. I. Bukhtiyarov, A. V. Lavrenov, V. A. Likholobov, *Appl. Catal. A* **2014**, *469*, 472–482.
[33] L. Shi, G. M. Deng, W. C. Li, S. Miao, Q. N. Wang, W. P. Zhang, A. H. Lu, *Angew. Chem. Int. Ed.* **2015**, *54*, 13994–13998; *Angew. Chem.* **2015**, *127*, 14200–14204.
[34] S. Rimaz, L. Chen, A. Monzón, S. Kawi, A. Borgna, *Chem. Eng. J.* **2021**, *405*, 126656.
[35] L.-L. Long, W.-Z. Lang, X. Liu, C.-L. Hu, L.-F. Chu, Y.-J. Guo, *Chem. Eng. J.* **2014**, *257*, 209–217.
[36] L. Bai, Y. Zhou, Y. Zhang, H. Liu, M. Tang, *Catal. Lett.* **2009**, *129*, 449–456.
[37] C. K. S. Choong, L. Huang, Z. Zhong, J. Lin, L. Hong, L. Chen, *Appl. Catal. A* **2011**, *407*, 155–162.
[38] Y. H. Taufiq-Yap, H. V. Lee, R. Yunus, J. C. Juan, *Chem. Eng. J.* **2011**, *178*, 342–347.
[39] W. Sinkler, S. I. Sanchez, S. A. Bradley, J. Wen, B. Mishra, S. D. Kelly, S. R. Bare, *ChemCatChem* **2015**, *7*, 3779–3787.
[40] J. Ke, W. Zhu, Y. Jiang, R. Si, Y.-J. Wang, S.-C. Li, C. Jin, H. Liu, W.-G. Song, C.-H. Yan, Y.-W. Zhang, *ACS Catal.* **2015**, *5*, 5164–5173.
[41] Z. Wu, B. C. Bukowski, Z. Li, C. Milligan, L. Zhou, T. Ma, Y. Wu, Y. Ren, F. H. Ribeiro, W. N. Delgass, J. Greeley, G. Zhang, J. T. Miller, *J. Am. Chem. Soc.* **2018**, *140*, 14870–14877.
[42] B. Qiao, A. Wang, X. Yang, L. F. Allard, Z. Jiang, Y. Cui, J. Liu, J. Li, T. Zhang, *Nat. Chem.* **2011**, *3*, 634–641.
[43] A. Virnovskaia, S. Jørgensen, J. Hafizovic, Ø. Prytz, E. Kleimenov, M. Hävecker, H. Bluhm, A. Knop-Gericke, R. Schlögl, U. Olsbye, *Surf. Sci.* **2007**, *601*, 30–43.
[44] K. Balakrishnan, *J. Catal.* **1991**, *127*, 287–306.
[45] J.-C. Dupin, D. Gonbeau, P. Vinatier, A. Levasseur, *Phys. Chem. Chem. Phys.* **2000**, *2*, 1319–1324.
[46] J. Yu, R. Wang, S. Ren, X. Sun, C. Chen, Q. Ge, W. Fang, J. Zhang, H. Xu, D. S. Su, *ChemCatChem* **2012**, *4*, 1376–1381.
[47] L. Deng, H. Miura, T. Shishido, S. Hosokawa, K. Teramura, T. Tanaka, *Chem. Commun.* **2017**, *53*, 6937–6940.
[48] B. Zhang, H. Asakura, J. Zhang, J. Zhang, S. De, N. Yan, *Angew. Chem. Int. Ed.* **2016**, *55*, 8319–8323; *Angew. Chem.* **2016**, *128*, 8459–8463.
[49] L. G. Cesar, C. Yang, Z. Lu, Y. Ren, G. Zhang, J. T. Miller, *ACS Catal.* **2019**, *9*, 5231–5244.